

11. Shen, Z.-X., Spicer, W. E., King, D. M., Dessau, D. S. & Wells, B. O. Photoemission studies of high- $T_c$  superconductors: The superconducting gap. *Science* **267**, 343–350 (1995).
12. Damascelli, A., Shen, Z.-X. & Hussain, Z. Angle-resolved photoemission spectroscopy of the cuprate superconductors. Preprint at (arXiv.org/cond-mat/0208504) (2002).
13. Campuzano, J. C., Norman, M. R. & Randeria, M. Photoemission in the high  $T_c$  superconductors. Preprint at (arXiv.org/cond-mat/0209476) (2002).
14. Byers, J. M., Flatté, M. E. & Scalapino, D. J. Influence of gap extrema on tunneling conductance near an impurity in an anisotropic superconductor. *Phys. Rev. Lett.* **71**, 3363 (1993).
15. Wang, Q. & Lee, D.-H. Quasiparticle scattering interference in high temperature superconductors. *Phys. Rev. B* **67**, 020511 (2003).
16. Zhang, D. & Ting, C. S. Energy-dependent LDOS modulation in cuprate superconductors. *Phys. Rev. B* **67**, 020511 (2003).
17. Fedorov, A. V. *et al.* Temperature dependent photoemission studies of optimally doped  $\text{Bi}_2\text{Sr}_2\text{CaCu}_2\text{O}_{8+\delta}$ . *Phys. Rev. Lett.* **82**, 2179–2183 (1999).
18. Feng, D. L. *et al.* Signature of superfluid density in the single-particle excitation spectrum of  $\text{Bi}_2\text{Sr}_2\text{CaCu}_2\text{O}_{8+\delta}$ . *Science* **289**, 277–281 (2000).
19. Ding, H. *et al.* Coherent quasiparticle weight and its connection to high- $T_c$  superconductivity from angle-resolved photoemission. *Phys. Rev. Lett.* **87**, 227001 (2001).
20. Johnson, P. D. *et al.* Doping and temperature dependence of the mass enhancement observed in the cuprate  $\text{Bi}_2\text{Sr}_2\text{CaCu}_2\text{O}_{8+\delta}$ . *Phys. Rev. Lett.* **87**, 177007 (2001).
21. Lanzara, A. *et al.* Evidence for ubiquitous strong electron-phonon coupling in high-temperature superconductors. *Nature* **412**, 510–514 (2001).
22. Valla, T. *et al.* Evidence for quantum critical behavior in the optimally doped cuprate  $\text{Bi}_2\text{Sr}_2\text{CaCu}_2\text{O}_{8+\delta}$ . *Science* **285**, 2110–2113 (1999).
23. Hoffman, J. E. *et al.* A four unit cell periodic pattern of quasiparticle states surrounding vortex cores in  $\text{Bi}_2\text{Sr}_2\text{CaCu}_2\text{O}_{8+\delta}$ . *Science* **295**, 466–469 (2002).
24. Crommie, M. F., Lutz, C. P. & Eigler, D. M. Imaging standing waves in a two-dimensional electron gas. *Nature* **363**, 524 (1993).
25. Howald, C., Eisaki, H., Kaneko, N. & Kapitulnik, A. Coexistence of charged stripes and superconductivity in  $\text{Bi}_2\text{Sr}_2\text{CaCu}_2\text{O}_8 + d$ . Preprint at (arXiv.org/cond-mat/0201546) (2002).
26. Polkovnikov, A., Sachdev, S. & Vojta, M. Spin collective mode and quasiparticle contributions to STM spectra of d-wave superconductors with pinning. Preprint at (arXiv.org/cond-mat/0208334) (2002).
27. Podolsky, D. *et al.* Translational symmetry breaking in the superconducting state of the cuprates: Analysis of the quasiparticle density of states. Preprint at (arXiv.org/cond-mat/0204011) (2002).
28. Howald, C. *et al.* Periodic density of states modulations in superconducting  $\text{Bi}_2\text{Sr}_2\text{CaCu}_2\text{O}_{8+\delta}$ . *Phys. Rev. B* **67**, 014533 (2003).
29. Kivelson, S. A. *et al.* How to detect fluctuating order in the high-temperature superconductors. Preprint at (arXiv.org/cond-mat/0210683) (2002).
30. Campuzano, J. C. *et al.* Direct observation of particle-hole mixing in the superconducting state by angle-resolved photoemission. *Phys. Rev. B* **53**, R14737–R14740 (1996).

**Acknowledgements** We thank J. C. Campuzano, M. E. Flatté, P. Johnson, S. A. Kivelson, B. Lake, R. B. Laughlin, J. W. Loram, M. Norman, D. J. Scalapino, Z.-X. Shen, J. Tranquada and J. Zaanen for discussions and communications. This work was supported by an LDRD from the Lawrence Berkeley National Laboratory, the ONR, the NSF, and by Grant-in-Aid for Scientific Research on Priority Area (Japan), a COE grant from the Ministry of Education (Japan), and NEDO (Japan). J.E.H. is grateful for support from a Hertz Fellowship.

**Competing interests statement** The authors declare that they have no competing financial interests.

**Correspondence** and requests for materials should be addressed to J.C.D. (e-mail: jcdavis@ccmr.cornell.edu).

## A subfemtotesla multichannel atomic magnetometer

I. K. Kominis<sup>\*†</sup>, T. W. Kornack<sup>\*</sup>, J. C. Allred<sup>‡</sup> & M. V. Romalis<sup>\*</sup>

<sup>\*</sup> Department of Physics, Princeton University, Princeton, New Jersey 08544, USA  
<sup>‡</sup> Department of Physics, University of Washington, Seattle, Washington 98195, USA

The magnetic field is one of the most fundamental and ubiquitous physical observables, carrying information about all electromagnetic phenomena. For the past 30 years, superconducting quantum interference devices (SQUIDS) operating at 4 K have been unchallenged as ultrahigh-sensitivity magnetic field detectors<sup>1</sup>, with a sensitivity reaching down to 1 fT Hz<sup>-1/2</sup> (1 fT = 10<sup>-15</sup> T). They have enabled, for example, mapping of

the magnetic fields produced by the brain, and localization of the underlying electrical activity (magnetoencephalography). Atomic magnetometers, based on detection of Larmor spin precession of optically pumped atoms, have approached similar levels of sensitivity using large measurement volumes<sup>2,3</sup>, but have much lower sensitivity in the more compact designs required for magnetic imaging applications<sup>4</sup>. Higher sensitivity and spatial resolution combined with non-cryogenic operation of atomic magnetometers would enable new applications, including the possibility of mapping non-invasively the cortical modules in the brain. Here we describe a new spin-exchange relaxation-free (SERF) atomic magnetometer, and demonstrate magnetic field sensitivity of 0.54 fT Hz<sup>-1/2</sup> with a measurement volume of only 0.3 cm<sup>3</sup>. Theoretical analysis shows that fundamental sensitivity limits of this device are below 0.01 fT Hz<sup>-1/2</sup>. We also demonstrate simple multichannel operation of the magnetometer, and localization of magnetic field sources with a resolution of 2 mm.

Ultrasensitive magnetometers have found a wide range of applications, from condensed-matter experiments<sup>5</sup> and gravitational wave detection<sup>6</sup>, to detection of NMR signals<sup>7,8</sup>, studies of palaeomagnetism<sup>9</sup>, non-destructive testing<sup>10</sup>, and underwater ordinance detection<sup>11</sup>. However, the most notable application of magnetic field sensors has been in the area of biomagnetism<sup>12,13</sup>, that is, the detection of the weak magnetic fields produced by the human brain, heart and other organs. For example, measurements of the magnetic field produced by the brain are used to diagnose epilepsy, and to study neural responses to auditory and visual stimuli. Low-temperature superconducting quantum interference device (SQUID) sensors<sup>14–16</sup>, which so far have dominated all of the above-mentioned applications, have reached sensitivity levels of 0.9–1.4 fT Hz<sup>-1/2</sup> with a pick-up coil area of the order of 1 cm<sup>2</sup>. In the low-frequency range of interest for biomagnetic studies (<100 Hz) their noise is typically somewhat higher, whereas commercial SQUID magnetometers typically<sup>17</sup> have noise of about 5 fT Hz<sup>-1/2</sup>, partly due to magnetic noise generated by electrically conductive radiation-shielding of the liquid-helium dewars<sup>18</sup>.

Atomic magnetometers rely on a measurement of the Larmor precession of spin-polarized atoms in a magnetic field<sup>19</sup>. The fundamental, shot-noise-limited sensitivity of an atomic magnetometer is given by

$$\delta B = \frac{1}{\gamma \sqrt{n T_2 V t}} \quad (1)$$

where  $n$  is the number density of atoms,  $\gamma$  is their gyromagnetic ratio,  $T_2$  is the transverse spin relaxation time,  $V$  is the measurement volume, and  $t$  is the measurement time<sup>20</sup>. The value of  $\gamma$  in equation (1) depends on the details of the magnetometer operation. For a commonly used Zeeman transition with  $\Delta m = 1$ ,  $\gamma = g \mu_B / \hbar (2I + 1)$ , where  $I$  is the nuclear spin of the alkali metal,  $\mu_B$  is the Bohr magneton, and  $g \approx 2$ . In our magnetometer operating at zero field, the effective  $\gamma$  for sensitivity estimates is  $\gamma = g \mu_B / \hbar$  (equation (7) of ref. 21).

Most atomic magnetometers use a polarized alkali-metal vapour (K, Rb, Cs), and their transverse spin relaxation time is limited by spin-exchange collisions between alkali atoms. In one implementation of such a magnetometer<sup>3,22</sup>, the shot-noise sensitivity was estimated to be 0.3 fT Hz<sup>-1/2</sup> for a 500-cm<sup>3</sup> cell. In another state-of-the-art magnetometer<sup>2</sup>, the actual sensitivity was estimated to be 1.8 fT Hz<sup>-1/2</sup> with a bandwidth of about 1 Hz and a measurement volume of 1,800 cm<sup>3</sup>.

We recently demonstrated operation of a spin-exchange relaxation-free (SERF) magnetometer<sup>21</sup> where broadening due to spin-exchange collisions is completely eliminated by operating at a high alkali-metal density in a very low magnetic field. The remaining broadening is determined by spin-relaxation collisions, which transfer spin angular momentum to rotational momentum of

<sup>†</sup> Present address: Lawrence Berkeley National Laboratory, Berkeley, California 94720, USA.

atomic motion. They have much smaller cross-sections compared to spin exchange, yielding theoretical limits on magnetic field sensitivity below  $0.01 \text{ fT Hz}^{-1/2}$  in  $1 \text{ cm}^3$ . However, to realize such sensitivity in practical applications usually requires operating the device as a magnetic gradiometer to cancel common-mode magnetic field noise. Such operation is routinely used in SQUID detectors, but previous atomic gradiometers either used two identical magnetometers with a baseline of the order of 1 m (ref. 23) or had a relatively low magnetic field sensitivity of about  $4 \text{ pT Hz}^{-1/2}$  (ref. 4). By adding  $^4\text{He}$  buffer gas to the magnetometer cell we slow the diffusion of the K atoms, and demonstrate multichannel operation of the magnetometer with high sensitivity and adjacent channel spacing of only 3 mm. This allows us to cancel ambient magnetic field noise, and demonstrate magnetic source localization with high spatial resolution. In Fig. 1 we show the theoretical sensitivity of the magnetometer as a function of K density, including the effects of spin exchange and spin relaxation due to K–K and K–He collisions.

A diagram of the SERF magnetometer is shown in Fig. 2. Potassium atoms are spin-polarized by the pump laser along the  $\hat{z}$  direction. We operate the magnetometer with all three components of the magnetic field close to zero. In this regime, a small  $B_y$  field rotates the spin polarization into the  $\hat{x}$  direction (see the bottom inset in Fig. 2). The plane of the polarization of the probe beam is rotated in proportion to the  $\hat{x}$  component of the spin polarization. Using a multichannel photodetector, we simultaneously measure the polarization of the probe beam and, therefore, the  $B_y$  field, at several adjacent points. It can be shown that the signal is not sensitive to small changes in  $B_x$  and  $B_z$  fields, and the device operates as a vector magnetometer. By taking a linear combination of the signals, we can make measurements of the first- and higher-order gradients of the magnetic field.

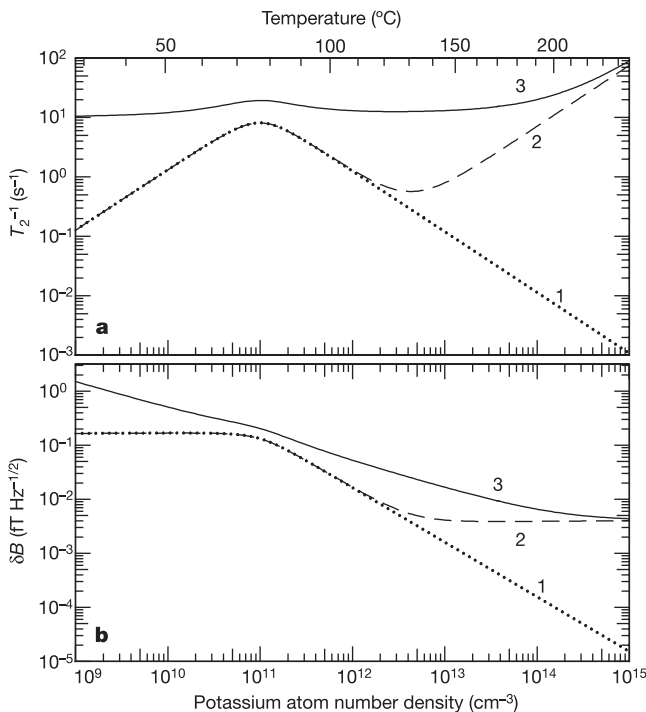


**Figure 1** Relaxation rate and theoretical magnetic field sensitivity. **a**, Transverse relaxation rate  $T_2^{-1}$  due to alkali metal spin-exchange collisions<sup>27</sup> in a small magnetic field  $B = 10 \mu\text{G}$  (case 1), spin-exchange and K–K spin-relaxation collisions (case 2), and the total transverse relaxation rate, also including the effect of K–He collisions for 2.9 atm of  $^4\text{He}$  gas (case 3). **b**, Estimated magnetic field sensitivity shot-noise limit for cases 1–3 obtained from equation (1) with a measurement volume  $V = 0.3 \text{ cm}^3$ .

The magnetic field sensitivity data are shown in Fig. 3a. The magnetometer frequency response (Fig. 3b) is measured by applying a known oscillating  $B_y$  field at several frequencies. The frequency response depends on the optical-pumping and spin-relaxation rates<sup>21</sup>, and is well described by a single-pole, low-pass filter with a cut-off frequency of about 20 Hz. The noise in a single magnetometer channel of about  $7 \text{ fT Hz}^{-1/2}$  (dashed line in Fig. 3a) is due to Johnson noise from our mu-metal shields with an inner diameter of 40 cm, and is consistent with estimates based on theoretical calculations<sup>18</sup>.

We form a first-order gradiometer by taking the difference between two adjacent magnetometer channels after correcting for a small difference in their absolute sensitivity. This procedure cancels the common magnetic field noise. Assuming that the remaining noise is uncorrelated, we divide the resulting noise level by  $\sqrt{2}$  to obtain the intrinsic magnetic field sensitivity of each channel (solid line in Fig. 3a). Apart from a number of sharp peaks from technical sources of noise, the magnetic sensitivity is less than  $1 \text{ fT Hz}^{-1/2}$  in the range 10–150 Hz, and averages to  $0.54 \text{ fT Hz}^{-1/2}$  in the range 28–45 Hz. To our knowledge, this represents the best magnetic field sensitivity obtained to date in

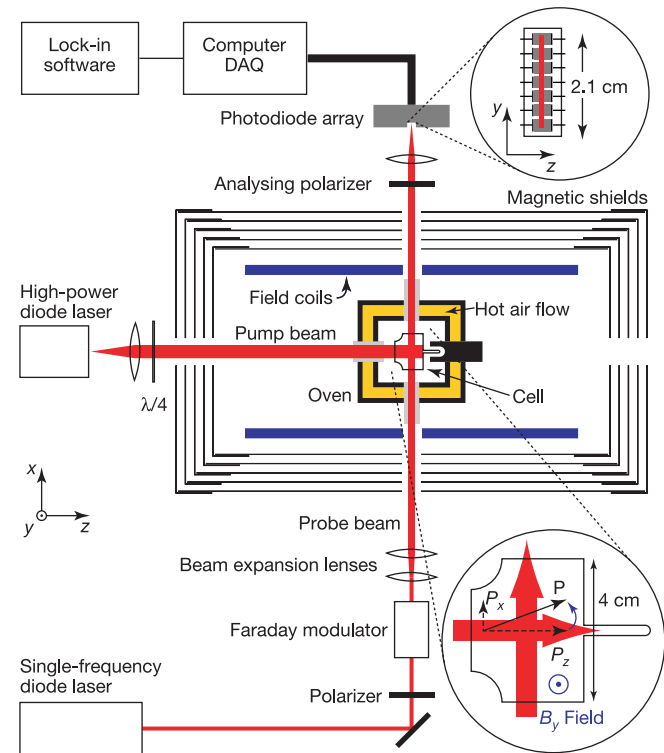


**Figure 2** Experimental set-up. The diagram shows: magnetic shields with a shielding factor of  $10^6$ ; field coils producing calibrated, uniform fields along  $\hat{x}, \hat{y}$  and  $\hat{z}$  directions, and all five independent first-order field gradients; a T-shaped glass cell ( $3 \times 4 \times 3 \text{ cm}$ ) with flat windows, containing a drop of K metal, 2.9 atm of  $^4\text{He}$  and 60 torr of  $\text{N}_2$ ; a double-wall oven heated to  $180 \text{ }^\circ\text{C}$  by flowing hot air to obtain a K atom number density of  $n \approx 6 \times 10^{13} \text{ cm}^{-3}$ ; a circularly polarized 1 W broadband diode laser ('pump' laser) tuned to the centre of the D1 line at 770 nm; a linearly polarized 100 mW single frequency laser ('probe' laser) detuned by 1 nm from the D1 resonance; a Faraday rotator modulating the plane of polarization of the probe laser with an amplitude  $\alpha \approx 0.02$  rad at a frequency  $f_{\text{mod}} = 2.9 \text{ kHz}$ ; beam-shaping optics that produce a collimated probe beam with a cross-section of  $4 \text{ mm} \times 19 \text{ mm}$ ; a polarization analyser, orthogonal to the polarizer; a seven-element photodiode array (shown in the top inset), with element separation of 0.31 cm along the  $\hat{y}$ -direction; and a 16-bit data acquisition system using a digital seven-channel lock-in amplifier to demodulate the signal proportional to the magnetic field  $B_y$ . Bottom inset, cross-section of the T-shaped cell, showing the rotation of the K polarization  $\mathbf{P}$  into the  $\hat{x}$  direction by an applied magnetic field  $B_y$ .

either superconducting or atomic magnetometers. The active measurement volume used by each channel is only 0.3 cm<sup>3</sup>.

The inset to Fig. 3b shows the magnetic noise in the difference between two channels as a function of the distance between them—that is, the baseline of the gradiometer. The probe beam slightly expands in the  $\hat{y}$  direction, so the channel spacing is 0.28 cm, 10% smaller than the photodiode element separation. We expect the noise to increase with the baseline  $d$  of the gradiometer owing to the magnetic field gradient noise. A fit of the form  $N = \sqrt{N_1^2 + N_2^2 + d^2 G^2}$ , where  $N_1$  and  $N_2$  are the intrinsic noise levels in each channel, gives a magnetic field gradient noise  $G = 1 \text{ fT cm}^{-1} \text{ Hz}^{-1/2}$ , which is somewhat larger than our estimate of  $0.5 \text{ fT cm}^{-1} \text{ Hz}^{-1/2}$  for the gradient noise produced by the magnetic shields<sup>18</sup>. This probably indicates that some noise comes from local sources—perhaps the metal in the temperature sensor near the cell. We can also form a second-order gradiometer using three adjacent channels. We find that the intrinsic sensitivity of each channel measured in this way is slightly better, but the improvement is not significant.

We also investigated the performance of the magnetometer in a multichannel imaging mode. We first apply a uniform oscillating magnetic field gradient  $dB_y/dy$  to check the linearity of the device (Fig. 4a). With the exception of the outer channels, which are not fully illuminated by the pump laser, the response is quite linear, and

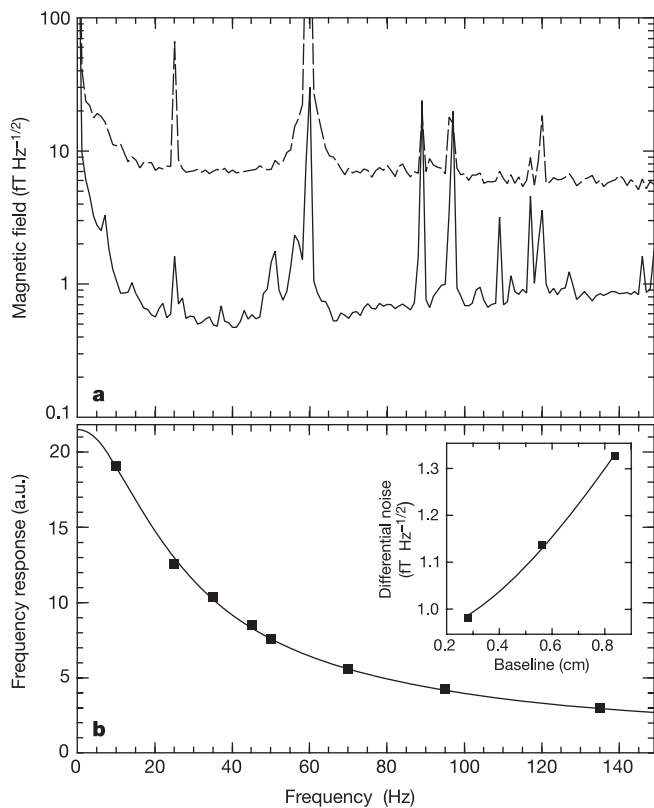


**Figure 3** Magnetic field sensitivity and bandwidth of the magnetometer. Magnetic field noise in a single channel (**a**, dashed line), and intrinsic magnetic field sensitivity of a single channel extracted from the difference between adjacent channels (**a**, solid line). The magnetic field sensitivity data are obtained by recording the response of the magnetometer for about 100 s, performing a fast Fourier transform (FFT) without windowing; and calculating r.m.s. amplitudes in 1 Hz bins. A peak due to the calibrating  $B_y$  field is seen at 25 Hz. To obtain absolute field sensitivity, we divide the magnetometer FFT by a normalized frequency-response function shown in **b** with a fit to  $A/(f^2 + B^2)^{1/2}$ , where the bandwidth  $B = 20$  Hz. Inset, magnetic field noise in the channel difference as a function of the distance between channels. The fit assumes that the noise increases owing to contributions from magnetic field gradient noise. a.u., arbitrary units.

the measured gradient agrees to within 4% with the strength of the applied gradient. To simulate a biological source, we place a small coil about 5.3 cm from the centre of the magnetometer. We apply an oscillating current to the coil with a frequency of 25 Hz, and analyse the data in 1-s intervals (Fig. 4b). We fit the data to the magnetic dipolar field profile, and find that after 1 s of averaging the uncertainty in the distance to the dipole is 2 mm and the uncertainty in its absolute size is 13%.

The spatial resolution of the magnetic field measurements inside the magnetometer cell is limited by the diffusion of the K atoms. On the basis of a detailed model of diffusion, we determine the resolution to be about 2 mm for our conditions, slightly smaller than the spacing between the channels. The accuracy of localization of magnetic field sources outside the magnetometer depends on a number of factors, including the signal-to-noise ratio, the distance from the magnetometer, and the uniformity of the magnetometer response. Typically, the magnetic field sources can be localized to a fraction of the detector size, so localization uncertainty of the order of 0.2 mm can be expected in our magnetometer for sufficiently high signal-to-noise ratio.

In addition to its high sensitivity, the SERF magnetometer described here does not require cryogenic cooling, making it very attractive for a wide range of applications, particularly outside laboratory environments. The bandwidth and size of the magnetometer are well suited for detection of biological fields. Two technical modifications would be needed to use the magnetometer for magnetoencephalography (MEG). First, the magnetometer would have to be placed in larger magnetic shields (similar to the magnetically shielded rooms at present used for MEG with SQUID magnetometers<sup>24</sup>), so as to accommodate a patient inside the shields. Second, more efficient thermal insulation and active cooling

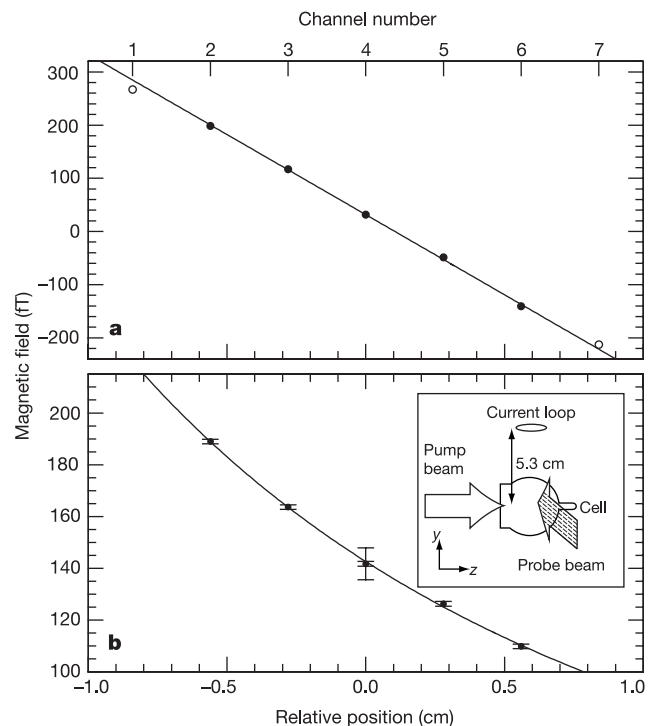


**Figure 4** Magnetic gradient imaging. **a**, Measured response for an applied uniform gradient  $dB_y/dy = 315 \text{ fT cm}^{-1}$  oscillating at 25 Hz. Only data represented by filled symbols are used in the linear fit, which gives a slope of  $301 \text{ fT cm}^{-1}$ . **b**, Measured response from a magnetic dipole  $\mu = 1.25 \text{ uA cm}^{-2}$  located 5.3 cm away and oscillating at 25 Hz, with the magnetic dipole field fit. The large error bar on the middle data point represents the single-channel noise level after 1 s of integration. The small error bars represent the noise in the relative signal between adjacent channels.

would also be needed, to keep the outside surface of the sensor at room temperature.

Our magnetometer is in a very early stage of development, and many improvements are possible. For example, by using a two-dimensional photodiode array it should be possible to measure gradients and localize sources in two directions. The overall noise of the magnetometer could be further reduced by using superconducting shields, which do not have a Johnson noise component. In the absence of Johnson noise, simple averaging of the existing channels would yield a sensitivity of  $0.2 \text{ fT Hz}^{-1/2}$ . With more optimization, such as increased probe laser power and increased K atom density, it should be possible to approach the shot-noise-limited sensitivity in the range  $10^{-2}$ – $10^{-3} \text{ fT Hz}^{-1/2}$ . The thermal magnetic noise produced by the brain<sup>25</sup> is of the order of  $0.1 \text{ fT Hz}^{-1/2}$ , so an optimized version of this magnetometer should enable the maximum possible amount of information to be obtained about brain electrical activity. This may enable non-invasive studies of individual cortical modules in the brain<sup>26</sup>, which have a size of 0.1–0.2 mm. □

Received 24 October 2002; accepted 4 February 2003; doi:10.1038/nature01484.

1. Weinstock, H. (ed.) *SQUID Sensors: Fundamentals, Fabrication and Applications* (Kluwer Academic, Dordrecht, 1996).
2. Aleksandrov, E. B. *et al.* Laser pumping in the scheme of an  $M_x$ -magnetometer. *Optics Spectrosc.* **78**, 292–298 (1995).
3. Budker, D., Kimball, D. F., Rochester, S. M., Yashchuk, V. V. & Zolotarev, M. Sensitive magnetometry based on non-linear magneto-optical rotation. *Phys. Rev. A* **62**, 043403 (2000).
4. Affolderbach, C., Stähler, M., Knappe, S. & Wynands, R. An all-optical, high sensitivity magnetic gradiometer. *Appl. Phys. B* **75**, 605–612 (2002).
5. Tsuei, C. C. & Kirtley, J. R. Phase-sensitive evidence for d-wave pairing symmetry in electron-doped cuprate superconductors. *Phys. Rev. Lett.* **85**, 182–185 (2000).
6. Harry, G. M., Jin, I., Paik, H. J., Stevenson, T. R. & Wellstood, F. C. Two-stage superconducting-quantum-interference-device amplifier in a high-Q gravitational wave transducer. *Appl. Phys. Lett.* **76**, 1446–1448 (2000).
7. Greenberg, Ya. S. Application of superconducting quantum interference devices to nuclear magnetic resonance. *Rev. Mod. Phys.* **70**, 175–222 (1998).
8. McDermott, R. *et al.* Liquid-state NMR and scalar couplings in microtesla magnetic fields. *Science* **295**, 2247–2249 (2002).
9. Kirschvink, J. L., Maine, A. T. & Vali, H. Paleomagnetic evidence of a low-temperature origin of carbonate in the Martian meteorite ALH84001. *Science* **275**, 1629–1633 (1997).
10. Tralshawala, N., Claycomb, J. R. & Miller, J. H. Practical SQUID instrument for non-destructive testing. *Appl. Phys. Lett.* **71**, 1573–1575 (1997).
11. Clem, T. R. Superconducting magnetic gradiometers for underwater target detection. *Naval Engineers J.* **110**, 139–149 (1998).
12. Hämaläinen, M. *et al.* Magnetoencephalography—theory, instrumentation, and applications to non-invasive studies of the working human brain. *Rev. Mod. Phys.* **65**, 413–497 (1993).
13. Rodriguez, E. *et al.* Perception's shadow: long-distance synchronization of human brain activity. *Nature* **397**, 430–433 (1999).
14. Zimmerman, J. E., Thiene, P. & Harding, J. T. Design and operation of stable RF-biased superconducting point-contact quantum devices, and a note on properties of perfectly clean metal contacts. *J. Appl. Phys.* **41**, 1572–1580 (1970).
15. Drung, D., Bechstein, S., Franke, K. P., Scheiner, M. & Schurig, T. Improved direct-coupled dc SQUID read-out electronics with automatic bias voltage tuning. *IEEE Trans. Appl. Supercond.* **11**, 880–883 (2001).
16. Oukhanski, N., Stolz, R., Zakosarenko, V. & Meyer, H. G. Low-drift broadband directly coupled dc SQUID read-out electronics. *Physica C* **368**, 166–170 (2002).
17. Del Gratta, C., Pizzella, V., Tecchio, F. & Romani, G. L. Magnetoencephalography—a noninvasive brain imaging method with 1 ms time resolution. *Rep. Prog. Phys.* **64**, 1759–1814 (2001).
18. Nenonen, J., Montonen, J. & Katila, T. Thermal noise in biomagnetic measurements. *Rev. Sci. Instrum.* **67**, 2397–2405 (1996).
19. Dupont-Roc, J., Haroche, S., Cohen-Tannoudji, C. Detection of very weak magnetic fields ( $10^{-9}$  gauss) by  $^{87}\text{Rb}$  zero-field level crossing resonances. *Phys. Lett. A* **28**, 638–639 (1969).
20. Budker, D. *et al.* Resonant nonlinear magneto-optical effects in atoms. *Rev. Mod. Phys.* **74**, 1153–1201 (2002).
21. Allred, J. C., Lyman, R. N., Kornack, T. W. & Romalis, M. V. High-sensitivity atomic magnetometer unaffected by spin-exchange relaxation. *Phys. Rev. Lett.* **89**, 130801 (2002).
22. Budker, D., Yashchuk, V. & Zolotarev, M. Nonlinear magneto-optic effects with ultra-narrow widths. *Phys. Rev. Lett.* **81**, 5788–5791 (1998).
23. Alexandrov, E. B., Balabas, M. V., Pasgalev, A. S., Vershovskii, A. K. & Yakobson, N. N. Double-resonance atomic magnetometers: From gas discharge to laser pumping. *Laser Phys.* **6**, 244–251 (1996).
24. Kadori, A., Miyashita, T. & Tsukada, K. Cancellation technique of external noise inside a magnetically shielded room used for biomagnetic measurements. *Rev. Sci. Instrum.* **71**, 2184–2190 (2000).
25. Varpula, T. & Poutanen, T. Magnetic field fluctuations arising from thermal motion of electric charge in conductors. *J. Appl. Phys.* **55**, 4015–4021 (1984).
26. Ts'o, D. Y., Frostig, R. D., Lieke, E. E. & Grinvald, A. Functional organization of primate visual cortex revealed by high-resolution optical imaging. *Science* **249**, 417–420 (1990).
27. Happer, W. & Tam, A. C. Effect of rapid spin exchange on the magnetic-resonance spectrum of alkali vapors. *Phys. Rev. A* **16**, 1877–1991 (1977).

**Acknowledgements** This work was supported by the NIH, the Packard Foundation and Princeton University.

**Competing interests statement** The authors declare that they have no competing financial interests.

**Correspondence** and requests for materials should be addressed to M.R. (e-mail: romalis@princeton.edu).

## Single-crystal gallium nitride nanotubes

Joshua Goldberger\*, Rongrui He\*, Yanfeng Zhang†, Sangkwon Lee†, Haoquan Yan\*, Heon-Jin Choi† & Peidong Yang\*†

\* Department of Chemistry, University of California, Berkeley, California 94720, USA

† Materials Science Division, Lawrence Berkeley National Laboratory, Berkeley, California 94720, USA

Since the discovery of carbon nanotubes in 1991 (ref. 1), there have been significant research efforts to synthesize nanometre-scale tubular forms of various solids<sup>2–10</sup>. The formation of tubular nanostructure generally requires a layered or anisotropic crystal structure<sup>2–4</sup>. There are reports<sup>5,6,11</sup> of nanotubes made from silica, alumina, silicon and metals that do not have a layered crystal structure; they are synthesized by using carbon nanotubes and porous membranes as templates, or by thin-film rolling. These nanotubes, however, are either amorphous, polycrystalline or exist only in ultrahigh vacuum<sup>8</sup>. The growth of single-crystal semiconductor hollow nanotubes would be advantageous in potential nanoscale electronics, optoelectronics and biochemical-sensing applications. Here we report an 'epitaxial casting' approach for the synthesis of single-crystal GaN nanotubes with inner diameters of 30–200 nm and wall thicknesses of 5–50 nm. Hexagonal ZnO nanowires were used as templates for the epitaxial overgrowth of thin GaN layers in a chemical vapour deposition system. The ZnO nanowire templates were subsequently removed by thermal reduction and evaporation, resulting in ordered arrays of GaN nanotubes on the substrates. This templating process should be applicable to many other semiconductor systems.

We grew arrays of ZnO nanowires on (110) sapphire wafers using a vapour deposition process developed in our laboratory<sup>12</sup>. These ZnO nanowire arrays were placed inside a reaction tube for GaN chemical vapour deposition. Trimethylgallium and ammonia were used as precursors, and were fed into the system with argon or nitrogen carrier gas. The deposition temperature was set at 600–700 °C. After the GaN deposition, the samples were treated at 600 °C with 10% H<sub>2</sub> in argon to remove the ZnO nanowire templates.

Figure 1a shows a scanning electron microscopy (SEM) image of the starting ZnO nanowire array templates. These nanowires have uniform lengths of 2–5 μm and diameters of 30–200 nm. They are well faceted with hexagonal cross-sections (Fig. 1a inset), exhibiting {110} planes on the sides. After the GaN deposition and template removal, the colour of the sample turns from white to yellowish or darker. The morphology of the initial nanowire arrays was maintained (Fig. 1b), except for the increase in the diameters of the resulting nanostructures. The nanostructures appear less faceted than the starting ZnO nanowire template. Compositional analysis on the final product shows little Zn signal. X-ray diffraction (XRD) on the sample shows only (00l) diffraction peaks of the